Revisiting the use of the immersed-boundary lattice-Boltzmann method for simulations of suspended particles

Mountrakis, L.; Lorenz, E.; Hoekstra, A.G.

DOI
10.1103/PhysRevE.96.013302

Publication date
2017

Document Version
Final published version

Published in
Physical Review E

Revisiting the use of the immersed-boundary lattice-Boltzmann method for simulations of suspended particles

L. Mountrakis, E. Lorenz,[*] and A. G. Hoekstra[†]

Computational Science Lab, Institute of Informatics, University of Amsterdam, Sciencepark 904, 1098 XH Amsterdam, The Netherlands

(Received 10 February 2017; published 5 July 2017)

The immersed-boundary lattice-Boltzmann method (IB-LBM) is increasingly being used in simulations of dense suspensions. These systems are computationally very expensive and can strongly benefit from lower resolutions that still maintain the desired accuracy for the quantities of interest. IB-LBM has a number of free parameters that have to be defined, often without exact knowledge of the tradeoffs, since their behavior in low resolutions is not well understood. Such parameters are the lattice constant Δx, the number of vertices N_v, the interpolation kernel ϕ, and the LBM relaxation time τ. We investigate the effect of these IB-LBM parameters on a number of straightforward but challenging benchmarks. The systems considered are (a) the flow of a single sphere in shear flow, (b) the collision of two spheres in shear flow, and (c) the lubrication interaction of two spheres. All benchmarks are performed in three dimensions. The first two systems are used for determining two effective radii: the hydrodynamic radius r_{hyd} and the particle interaction radius r_{inter}. The last system is used to establish the numerical robustness of the lubrication forces, used to probe the hydrodynamic interactions in the limit of small gaps. Our results show that lower spatial resolutions result in larger hydrodynamic and interaction radii, while surface densities should be chosen above two vertices per LU^2 result to prevent fluid penetration in underresolved meshes. Underresolved meshes also failed to produce the migration of particles toward the center of the domain due to lift forces in Couette flow, mostly noticeable for IBM-kernel ϕ_2. Kernel ϕ_4, despite being more robust toward mesh resolution, produces a notable membrane thickness, leading to the breakdown of the lubrication forces in larger gaps, and its use in dense suspensions where the mean particle distances are small can result in undesired behavior. r_{hyd} is measured to be different from r_{inter}, suggesting that there is no consistent measure to recalibrate the radius of the suspended particle.

DOI: 10.1103/PhysRevE.96.013302

I. INTRODUCTION

The immersed-boundary method (IBM) is a pure fluid-structure interaction method that has been used in a wide range of applications [1–8]. Many variations of the IBM have been presented since its original introduction by Peskin in 1972 [9,10]. Uhlmann [11] suggested an improved version of the IBM with a direct formulation of the fluid-solid interaction force, using the regularized δ function to associate arbitrary Lagrangian with discrete Eulerian positions. Kempe and Fröhlich [12] proposed several enhancements to Uhlmann's approach [11] to improve the range of stability of the method and to deal with approaching interfaces. Yang *et al.* [13] developed a smoothing technique for the discrete δ functions of the IBM to suppress the nonphysical oscillations in the volume forces, while Wu and Shu [14] presented a model that accurately satisfies the nonslip boundary condition at boundary points.

However, the initial formulation of the IBM is also widely used due to its simplicity [5,15,16]. The role of some key IBM parameters and their effect on the interactions between the fluid and the immersed structure, or between the immersed structures, is not fully understood in either the initial formulation or the improved versions. Krüger *et al.* [17] investigated the impact of some of these relevant parameters by looking into the deformation of an initially spherical capsule, freely suspended in a simple shear flow. They found that the tessellation method and resolution of the membrane mesh play only a minor role, while the width of the discrete δ function significantly affected the results of their simulations.

The IBM is often combined with the lattice-Boltzmann method (LBM) as the fluid solver, a combination known as the immersed-boundary lattice-Boltzmann method (IB-LBM). The IB-LBM is widely used for the simulation of deformable particles, such as red blood cells (RBCs) [4–8,15,16] and capsules [17,18]. Due to their deformability, RBCs can pack very efficiently, resulting in blood suspensions with very high volume fraction in which the mean particle-particle distance is small.

To understand the role of IB-LBM parameters in particle-particle interactions, we performed an extensive study of their impact on a set of demanding benchmarks. The parameters considered are the interpolation kernel ϕ_n, the grid resolution Δx, the number of vertices used to represent a suspended particle, N_v, and the LBM relaxation parameter τ. The basic IBM implementation is used with stiff spherical particles, and any deviation from the spherical shape is being tracked. Many analytical solutions and reference tests exist or can be constructed for solid spheres [19–24], rendering them the most tractable shape for our simulations. We use the same version of the IB-LBM as the ones used in our deformable particle simulations [5,6,15] to study the behavior and shortcomings of the approach, yet in the stiff limit to approximate solid spheres. We are not using a variant for solid objects, since our aim is to study the behavior of the IBM, and spheres provide a clean method to do so. The benchmark systems are (a) a single sphere

[*]Also at Electric Ant Lab, Amsterdam, The Netherlands.

[†]Author to whom all correspondence should be addressed: A.G.Hoekstra@uva.nl; also at ITMO University, Saint-Petersburg, Russian Federation.

in shear flow, determining its effective hydrodynamic volume by measuring Einstein's viscosity, (b) the collision of two particles in shear flow, and (c) the lubrication interaction of two spheres. All benchmarks are performed in three dimensions.

In the appendixes, we provide supporting material for the results presented in the paper.

II. METHODS

A combined immersed-boundary lattice-Boltzmann method is employed to couple the suspended spheres with the fluid. The constitutive model used in the following simulations is the same as for red blood cells (RBCs) [15], yet much stiffer. Spheres are chosen for the simulations due to the existence of benchmark tests and known analytical results. The departure from the spherical shape is being tracked and ensured to be within acceptable limits (less than 1% of the radius). More information can be found in Appendix B.

A. Lattice-Boltzmann method

The lattice-Boltzmann method (LBM) is a well-established mesoscopic approach that solves asymptotically the incompressible Navier-Stokes equation [25]. The LBM's main quantity is the set of populations $f_i(\mathbf{x},t)$, which corresponds to the discretized probability distribution of finding particles in site $\mathbf{x}$, at time t, moving with velocity $\mathbf{c}_i$.

The time evolution of the distributions, when an external force is involved, is given by the forced single-relaxation time LBGK equation [25,26],

$$f_i(\mathbf{x}+\mathbf{c}_i\Delta t, t+\Delta t) = f_i(\mathbf{x},t) - \frac{f_i(\mathbf{x},t) - f_i^{\mathrm{eq}}(\mathbf{x},t)}{\tau} + \Delta t F_i, \quad (1)$$

where τ is the relaxation parameter, Δt is the time step, $f_i^{\mathrm{eq}}(\mathbf{x},t)$ is the equilibrium population, and F_i is the forcing term.

The equilibrium populations are given by

$$f_i^{\mathrm{eq}}(\mathbf{x},t) = w_i\rho\left[1 + \frac{\mathbf{u}\cdot\mathbf{c}_i}{c_s^2} + \frac{1}{2}\left(\frac{\mathbf{u}\cdot\mathbf{c}_i}{c_s^2}\right)^2 - \frac{u^2}{2c_s^2}\right], \quad (2)$$

where w_i is the weighting factor, ρ and $\mathbf{u}$ are the fluid density and velocity, respectively, and $c_s = \frac{1}{\sqrt{3}}\Delta x/\Delta t$ is the lattice speed of sound.

The zeroth and first moments of the populations recover the fluid density $\rho = \sum_i f_i$ and velocity $\rho\mathbf{u} = \sum_i f_i\mathbf{c}_i + \frac{\Delta t}{2}\mathbf{f}$, while the kinematic viscosity ν of the fluid is given by $\nu = (\tau - \frac{1}{2})c_s^2\Delta t$. The forcing term F_i of Eq. (1) is in the form of

$$F_i = \left(1 - \frac{1}{2\tau}\right)w_i\left(\frac{\mathbf{c}_i - \mathbf{u}}{c_s^2} + \frac{(\mathbf{c}_i\cdot\mathbf{u})}{c_s^4}\mathbf{c}_i\right)\cdot\mathbf{f}, \quad (3)$$

where $\mathbf{f}$ is the external body force density.

We used the so-called D3Q19 model (three-dimensional with 19 velocity components) as implemented in the open-source LBM-solver Palabos [15,27] and built the IBM and the constitutive model on top of it.

B. Constitutive model of a cell membrane

We employ the spectrin-link model [28,29], widely used in red blood cell simulations and carefully parametrized in this study to correspond to a near-rigid sphere. Each sphere consists of a network of vertices, forming a triangular mesh.

The Helmholtz free energy of the system is given by

$$F(\{\mathbf{x}_n\}) = F_{\text{in-plane}} + F_{\text{bending}} + F_{\text{volume}} + F_{\text{area}}, \quad (4)$$

where $\mathbf{x}_n, n \in 1,\ldots,N_v$ are the vertices of a two-dimensional triangulated network describing the surface of a sphere.

The in-plane free-energy term is written as

$$F_{\text{in-plane}} = k_{\mathrm{WLC}}\left(\sum_{l\in\text{edges}} V_{\mathrm{WLC}}(L_l) + \sum_{l\in\text{edges}}\frac{k_{\mathrm{rep}}}{L_l}\right), \quad (5)$$

$$\text{with} \qquad V_{\mathrm{WLC}}(L_l) = \frac{k_B T L_{\max}}{4p}\frac{3x_l^2 - 2x_l^3}{1 - x_l}. \quad (6)$$

V_{WLC} is the wormlike chain potential, L_l is the length of the edge l, $L_{\max}$ is the maximum allowed extension length, x_l is defined as $x_l = \frac{L_l}{L_{\max}}$, p is the persistence length, and k_{rep} is a constant chosen so that the corresponding in-plane force is zero for the equilibrium length L_0. k_B is Boltzmann's constant, and $T = 300$ K is the temperature.

The bending energy is defined as

$$F_{\text{bending}} = \sum_{\text{adjacent }\alpha,\beta\text{ pair}} k_{\mathrm{bend}}[1 - \cos\{\theta_{\alpha\beta} - \theta_0\}], \quad (7)$$

where k_{bend} is the bending constant, and $\theta_{\alpha\beta}$ and θ_0 are the instantaneous and equilibrium angles between two adjacent triangles, respectively.

The volume and surface conservation constraints are written as

$$F_{\text{volume}} = k_{\text{volume}}\frac{k_B T}{2L_0^3}\frac{(\Omega - \Omega_0)^2}{\Omega_0}, \quad (8)$$

$$F_{\text{area}} = k_{\text{surface}}\frac{k_B T}{2L_0^2}\frac{(S - S_0)^2}{S_0} + \sum_{k\in 1,\ldots,\mathrm{N_t}} k_{\text{shear}}\frac{k_B T}{2L_0^2}\frac{(A_k - A_0)^2}{A_0}, \quad (9)$$

in which k_{volume}, k_{surface}, and k_{shear} are volume, surface, and local triangle area constants. Ω, S, and A_k are the volume, surface, and triangle area of the cell, while Ω_0, S_0, and A_0 are the corresponding equilibrium values.

The force acting on vertex i is derived from $\mathbf{f}_i = -\frac{\partial F(\{\mathbf{x}_i\})}{\partial \mathbf{x}_i}$ and was calculated analytically.

The equilibrium quantities in Eqs. (5)–(9) are obtained from the initial shape and may differ per vertex and triangle. This ensures the absence of residual stresses in a similar fashion to the stress-free membrane model followed by Fedosov *et al.* [30]. The remaining simulation parameters, including those of the fluid, are shown in Table I. The density and viscosity ratio between the inner and the outer fluid is set to 1.

The mesh is obtained by subdividing a regular icosahedron or octahedron and mapping the points of the surface to a sphere, similar to [17] (see Table II). Applying a stretch force of 250 pN in the two poles of the sphere, similar to the stretching of an

TABLE I. Model parameters and constants.

Parameter	Value
fluid density, ρ	1025 kg/m^3
kinematic viscosity, ν	1.7×10^{-6} m^2/s
bending constant, k_{bend}	$2 \times 10^5 k_B T$
volume constant, k_{volume}	6×10^5
surface constant, k_{surface}	6×10^5
local area constant, k_{shear}	5×10^4
maximum edge length, $L_{\max}$	$1.1 \times L_0$
WLC coefficient, k_{WLC}	15

RBC [28], yields a deviation of less than 0.08% from the initial radius.

Considering the low particle-Reynolds numbers used in this study (see Sec. III), the spheres are rendered near-rigid; however, the departure from the spherical shape is tracked for every experiment. The particle-Reynolds number is defined as $\text{Re}_p = \frac{4\dot{\gamma} r^2}{\nu}$, where ν is the kinematic viscosity of the fluid, $\dot{\gamma}$ is the applied shear rate, and r is the radius of the sphere.

C. Immersed-boundary method

The immersed-boundary method (IBM) [9,10] is a pure coupling method used in fluid-structure interaction problems. The major advantage of the IBM is that the discretized representations of the fluid and the immersed structure do not need to conform. This alleviates the need for remeshing, rendering complex configurations like dense suspensions easier to handle.

The key principle behind the IBM is the no-slip condition at the interface of the membrane and the fluid. In the original method proposed by Peskin [9,10], also used here, this is achieved by pinning the membrane points to the fluid. This is attained as the fluid velocity is interpolated at the Lagrangian surface points and the computed forces are exerted to the fluid. The force $\mathbf{F}_i(t)$ computed at the surface point $\mathbf{x}_i(t)$ is distributed among the closest Eulerian points $\mathbf{X}$ of the fluid according to

$$\mathbf{f}(\mathbf{X},t) = \sum_i \mathbf{F}_i(t)\delta(\mathbf{X} - \mathbf{x}_i(t)), \tag{10}$$

TABLE II. Properties of spherical meshes, created by subdividing either a regular icosahedron or an octahedron. N_v corresponds to the number of vertices, N_t to the number of triangles, and the symbol σ to the standard deviation of the quantity denoted in the subscript (as used in Sec. II B). The regular icosahedron produces more homogeneous meshes; however, due to the constitutive model, there are no residual stresses resulting from an inhomogeneous mesh.

Initial shape	N_v	N_t	σ_{A_0}/A_0	$\sigma_{L_l}/\langle L_l \rangle$	$\sigma_{\theta_0}/\theta_0$
icosahedron	162	320	8.5%	6.4%	14.3%
octahedron	258	512	23.9%	14.9%	39.0%
icosahedron	642	1280	8.6%	6.5%	15.9%
octahedron	1026	2048	24.2%	15%	40.9%
icosahedron	2562	5120	8.6%	6.5%	16.6%

where $\delta(\mathbf{X} - \mathbf{x}_i(t))$ is the discrete Dirac delta function. $\mathbf{f}(\mathbf{X},t)$ is coupled to the LBM via the forcing term as described in Eq. (3).

Subsequently, the velocity of the membrane point i is updated based on the local flow field and advected according to the Euler scheme

$$\mathbf{x}_i(t + \Delta t) = \mathbf{x}_i(t) + \mathbf{u}_i(t + \Delta t)\Delta t \tag{11}$$

or to the Adams-Bashforth scheme

$$\mathbf{x}_i(t + \Delta t) = \mathbf{x}_i(t) + \left(\tfrac{3}{2}\mathbf{u}_i(t + \Delta t) - \tfrac{1}{2}\mathbf{u}_i(t)\right)\Delta t, \tag{12}$$

where

$$\mathbf{u}_i(t + \Delta t) = \sum_i \mathbf{u}(\mathbf{X},t + \Delta t)\delta(\mathbf{X} - \mathbf{x}_i(t)). \tag{13}$$

The function $\delta(\mathbf{r})$ of Eqs. (10) and (13), used for the velocity interpolation and force spreading, is replaced by a product of 1D interpolation kernel functions ϕ_n, where n denotes the support of the kernel in all directions, as $\delta(\mathbf{r}) = \phi_n(x)\phi_n(y)\phi_n(z)$, where $\mathbf{r} = (x,y,z)$. In the present work, we make use of the following kernels:

$$\phi_2(r) = \begin{cases} 1 - |r|, & |r| \leqslant 1, \\ 0, & 1 \leqslant |r|, \end{cases} \tag{14}$$

$$\phi_3(r) = \begin{cases} \frac{1}{3}(1 + \sqrt{1 - 3r^2}), & |r| \leqslant 1, \\ \frac{1}{6}(5 - 3|r| - \sqrt{-2 + 6|r| - 3r^2}), & \frac{1}{2} \leqslant |r| \leqslant \frac{3}{2}, \\ 0, & \frac{3}{2} \leqslant |r|, \end{cases} \tag{15}$$

$$\phi_4(r) = \begin{cases} \frac{1}{8}(3 - 2|r| + \sqrt{1 + 4|r| - 4r^2}), & |r| \leqslant 1, \\ \frac{1}{8}(5 - 2|r| - \sqrt{-7 + 12|r| - 4r^2}), & 1 \leqslant |r| \leqslant 2, \\ 0, & 2 \leqslant |r|. \end{cases} \tag{16}$$

The support of each kernel is shown in Fig. 1.

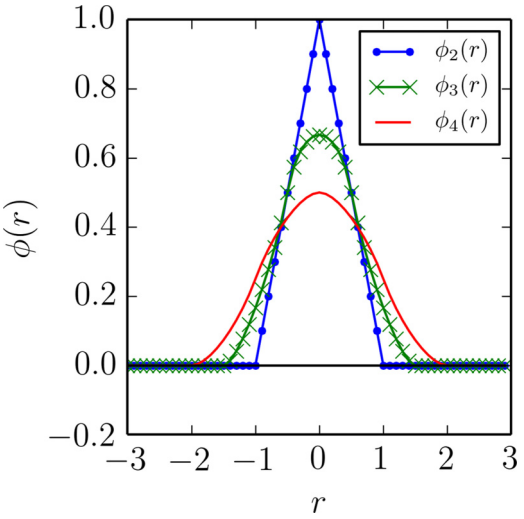

FIG. 1. Support functions for IBM kernels ϕ_2, ϕ_3, and ϕ_4 [Eqs. (14), (15), and (16), respectively].

Free parameters of the IB-LBM

The IBM comes with a number of free parameters. The most important are the interpolation kernel ϕ, the number of surface vertices N_v, the lattice discretization Δx, the update scheme [Eqs. (11) and (12)], and the LBM relaxation time τ. While it is implied that a finer spatial and mesh resolution, i.e., smaller Δx and more N_v, respectively, would yield more accurate results, the computationally demanding case of dense suspensions can significantly benefit from identifying the limits and the artifacts of each parameter.

The interpolation kernel ϕ is the core of the IBM. It introduces an artificial length scale, effectively changing the thickness of the membrane. It is known that kernel ϕ_2 [Eq. (14)] violates the translational invariance, and it has been found to introduce nonphysical oscillations [10,13], yet ϕ_2 is considered to capture the relevant physics and is still preferred due to its compact support (one Δx in each direction), small numerical thickness, and reduced amount of computations [6,17].

The number of surface vertices N_v has been found to play only a minor role [11,17], and a suggested mean vertex distance varies between 0.5 and $1.5\Delta x$ [17] (3D simulations) or $0.33\Delta x$ [6] (2D simulations) without compromising the impermeability of the particle membrane. The Euler update scheme is used more often in the literature, while Krüger [17] argues that higher-order schemes, such as the Adams-Bashforth scheme, will not change the outcome of short simulations, yet it might provide additional accuracy for longer-time simulations. The effect of the LBM relaxation time τ, on the other hand, has been found to be considerable on the IB-LBM simulations, in both simulations of capsules [17] and when acting as velocity boundaries [31]. It is also worth noting that τ has a similarly considerable effect on bounce-back boundaries.

III. SIMULATION RESULTS

We consider three representative cases, accounting for the interactions of IBM membranes with the fluid and with other IBM membranes. First, we look into the behavior of the effective hydrodynamic radius r_{hyd} of a sphere with radius r in a sheared environment. Next, we investigate the interaction between two particles in a sheared environment. As our final case, two spheres are forced to collide as we examine the gap h where lubrication forces break down.

All simulations correspond to the same system: a domain of $20r \times 20r \times 20r$ containing one or two spheres with a dimensional radius of 4 μm. The length and time scales are chosen for their relevance to red blood cell suspensions, which are of particular interest to our line of research, yet the results can be carried over to other systems following a similar dimensionless scaling. Dimensionless parameters used to characterize the system, such as Reynolds number and confinement, are fixed for all simulations in each benchmark. By using the same dimensional system, we highlight the differences imposed by choosing different IB-LBM parameters.

We use stiff spherical particles omitting additional interparticle forces, such as explicit lubrication or penetration correction, to capture the interactions arising purely from the IB-LBM. Finite-size effects were not considerable, i.e., they were less than 6% in all of the examined cases; see Appendix A.

TABLE III. Default parameter set used for the simulations, unless stated otherwise.

Parameter	Value
Lattice constant, Δx	1.0 μm
Radius of sphere, r	4.0 LU
Total number of vertices per sphere, N_v	258
Relaxation time, τ	1.0
IBM kernel, ϕ_n	ϕ_4
IBM update scheme	Euler

The default parameter set is shown in Table III, with each figure that follows explicitly denoting the parameters that were varied. Note that when the radius of the particle is varied, what actually changes is the lattice constant Δx, resulting in a different particle radius in lattice units. In other words, all simulations have the same dimensional radius, yet they differ in lattice resolution. In the cases in which the LBM relaxation parameter τ is changed, the time step changes according to the diffusive scaling relation $\Delta t = \frac{\nu_{\text{LB}}}{\nu}\Delta x^2$, where ν_{LB} is the lattice viscosity. The parameters of the membrane model presented in Table I have been scaled accordingly to correspond to the same dimensional system. Results are presented in two forms, dimensional and dimensionless, always denoting the unit: μm for dimensional and LU for lattice units.

A. Hydrodynamic radius of a sphere

Einstein's well-known relation $\nu_{\text{rel}} = 1 + 2.5\varphi_{\text{V}}$ connecting the relative apparent viscosity ν_{rel} of a dilute suspension with the volume fraction φ_{V} is a convenient way to measure the effective hydrodynamic radius of a sphere by measuring its volume. The effective hydrodynamic radius of a sphere is then measured as

$$r_{\text{hyd}} = \sqrt[3]{\frac{3}{4\pi}\varphi_{\text{V}} V}, \tag{17}$$

where V is the volume of the domain, equal to $(20r)^3$. The volume fraction is $\varphi_{\text{V}} = 0.0525\%$ and is well within the limits of Einstein's relation between volume fraction and apparent viscosity.

The hydrodynamic radius is a measure of the hydrodynamic size of the particle as felt by the fluid and the contribution of the particle to the viscosity of the suspension. It is not intended to be used as a recalibration parameter.

The imposed radius, the hydrodynamic radius, and their difference Δr_{hyd} are shown in Fig. 2(a). The maximum extent of r_{hyd} is defined by the support of the IBM kernel. For ϕ_4 this is ± 2 LU. Parameters such as the radius r of the sphere, the relaxation time τ, and the surface density of the vertices, N_v/S_{LU}, where S_{LU} is the surface of the sphere, control the actual extent of the radius.

The sphere is placed between two plates in a shear-flow environment, as depicted in Fig. 2(b). The fluid is initialized at rest. From the two parallel plates, only the top one is moving and the bottom measures the shear stress of the suspension via the momentum-exchange method [32]. The location of the bottom boundary wall is considered to be halfway between the bounce-back node and the first fluid node, since $\tau = 1.0$ [33].

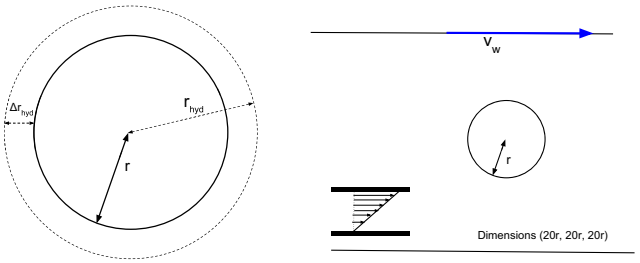

FIG. 2. Setup for measuring the hydrodynamic radius of a sphere. (a) Imposed radius r (solid lines) and effective hydrodynamic radius r_{hyd} (dashed lines). Their difference $\Delta r_{\mathrm{hyd}} = r_{\mathrm{hyd}} - r$ defines the deviation of the imposed radius from the measured one. (b) A sphere positioned in a shear flow environment at rest. The bottom plate is fixed and the suspension stress is measured via the momentum exchange algorithm.

To verify this approach, we perform fluid-only simulations and obtain a relative viscosity of $\nu_{\mathrm{rel}} = 1.0$. The applied shear rate is $\dot{\gamma} = 1000/\mathrm{s}$ and the particle-Reynolds number is $\mathrm{Re_p} = 0.038$.

Results

The effective hydrodynamic radius r_{hyd} is measured as the time average of $r_{\mathrm{hyd}}(t)$ from $\dot{\gamma}t = 10$ to 25, as shown in Fig. 3(a), while the error bars in the plots are defined as the standard deviation during this time period.

The hydrodynamic radii for dimensional and dimensionless units are shown in Figs. 3(a) and 3(b), respectively. Coarser spatial resolutions, where the radius of the sphere is expressed with fewer lattice units, result in an increased r_{hyd}. For example, a sphere radius of 8 LU appears increased by only ∼10%, while when $r = 2.7$ LU its increase is ∼35%, indicating the latter as a coarse representation.

Figures 3(b) and 3(c) contain the same data, yet they are plotted against different quantities. The spatial resolution dominates the increase, which, in absolute numbers, seems unaffected by the vertex density [inset of Fig. 3(c)]. For the cases $r = 4.0$, 5.0, and 8.0 LU, Fig. 3(c) shows that Δr_{hyd} is small for $N_v/S_{\mathrm{LU}} < \sim 2$ (and seemingly constant for $r = 8.0$ LU), and for $N_v/S_{\mathrm{LU}} > \sim 2$ it jumps to a higher value. This threshold is more visible for kernels with smaller support, such as ϕ_2 and ϕ_3 [Fig. 3(d)], while the increase in r_{hyd} for adequate mesh resolutions is independent of the IBM kernel used. The increase for underresolved meshes is almost half of that for the finer mesh resolutions, which may be due to the fluid penetrating the membrane. For the lower resolutions, this highlights that being closer to the input radius is not the desired outcome, but a consequence of the underresolved mesh. IBM kernel ϕ_4 is more robust in low mesh resolutions, counteracting what in ϕ_2 and ϕ_3 appears as membrane permeability. ϕ_4 has twice the support of ϕ_2, thus extending the reach of each vertex, allowing for meshes with fewer surface vertices to appear coherent.

It is also worth noting that the use of a higher-order scheme, such as the Adams-Bashforth scheme [Eq. (12)], had no impact on the results we obtained (data not shown).

B. Interaction between nearby membranes

1. Two spheres in shear flow

One important benchmark for transport studies is the interaction of two spheres in a simple shear-flow environment. Analytical solutions for this system have been derived by Batchelor and Green [19] for systems without boundaries and inertia. Depending on the initial distance of the two spheres, their trajectories can either extend to infinity or be finite, characterized as *open* or *closed* trajectories, respectively. In these open trajectories, two smooth spheres return to their original streamlines after a collision, where potential asymmetries between pre- and postcollision positions lead to shear-induced dispersion [20,21]. In bounded cases of Couette flow, a neutrally buoyant sphere migrates toward the center of the domain [34], and the origin of this migration lies in the interaction of the force dipole generated by the particle and its image in the wall [35].

We place two identical spheres in a linear shear-flow domain of size $(20r \times 20r \times 20r)$ and apply a shear rate of $\dot{\gamma} = 132.8/\mathrm{s}$, resulting in a particle-Reynolds number of $\mathrm{Re_p} = 0.005$, using the input radius. The initial distance between the two spheres is $(\Delta X_0, \Delta Y_0, \Delta Z_0) = (10r, 1.5r, 0)$, where the y direction is the shear-gradient direction. The setup is shown in Fig. 4.

We are interested in the collision distance in the y direction, $\Delta Y_{\mathrm{max}} \equiv \Delta Y_{\Delta X=0}$, which occurs when $\Delta X = 0$, and from that we define the interaction radius $r_{\mathrm{inter}} = \Delta Y_{\mathrm{max}}/2$. Under the assumption of smooth spheres and low Re_p, two spheres of equal size pass very close to each other, so that $\Delta Y_{\mathrm{max}} \to 2r$, while having symmetric pre- and postcollisional trajectories [19]. The increase in the interaction radius is measured as $\Delta r_{\mathrm{inter}} = r_{\mathrm{inter}} - r$. The increase $\Delta r_{\mathrm{inter}}$ is not a particle property and is used as a reference to study deviations that may vary between simulations.

2. Results

Figure 5 shows the parametric plots of $\Delta Y/r$ versus $\Delta X/r$ for varying mesh resolutions and $\tau = 1.5$. The migration of the spheres toward the center of the domain can be distinguished before and after the collision.

As shown in Figs. 6(a), 6(b) and 6(c), the interaction radius r_{inter} is systematically larger than the hydrodynamic radius r_{hyd} of the previous section. This result excludes the use of r_{hyd} as a parameter that can be used to recalibrate r in order to obtain more accurate results. With respect to mesh resolution, $\Delta r_{\mathrm{inter}}$ levels off above ∼1 vertex per LU for adequately resolved meshes [inset of Fig. 6(a)], contrary to Δr_{hyd}.

In this benchmark, choosing an interpolation kernel ϕ_n with a larger support increases the interaction radius while preserving the discrepancies between the underresolved and adequately resolved meshes [see Fig. 6(c)]. Increasing the relaxation time τ leads to decreasing r_{inter} [Fig. 6(d)]. A similar behavior was also observed by Nguyen and Ladd [22] for the momentum-exchange algorithm [32,36]. In this view, the IBM behaves similarly to the LBM's bounce-back boundaries, where the position of the boundary depends on the relaxation time τ [33].

One cannot help but notice the decrease in $\Delta Y/r$ before and after the collision in Fig. 5, which increases as N_v increase.

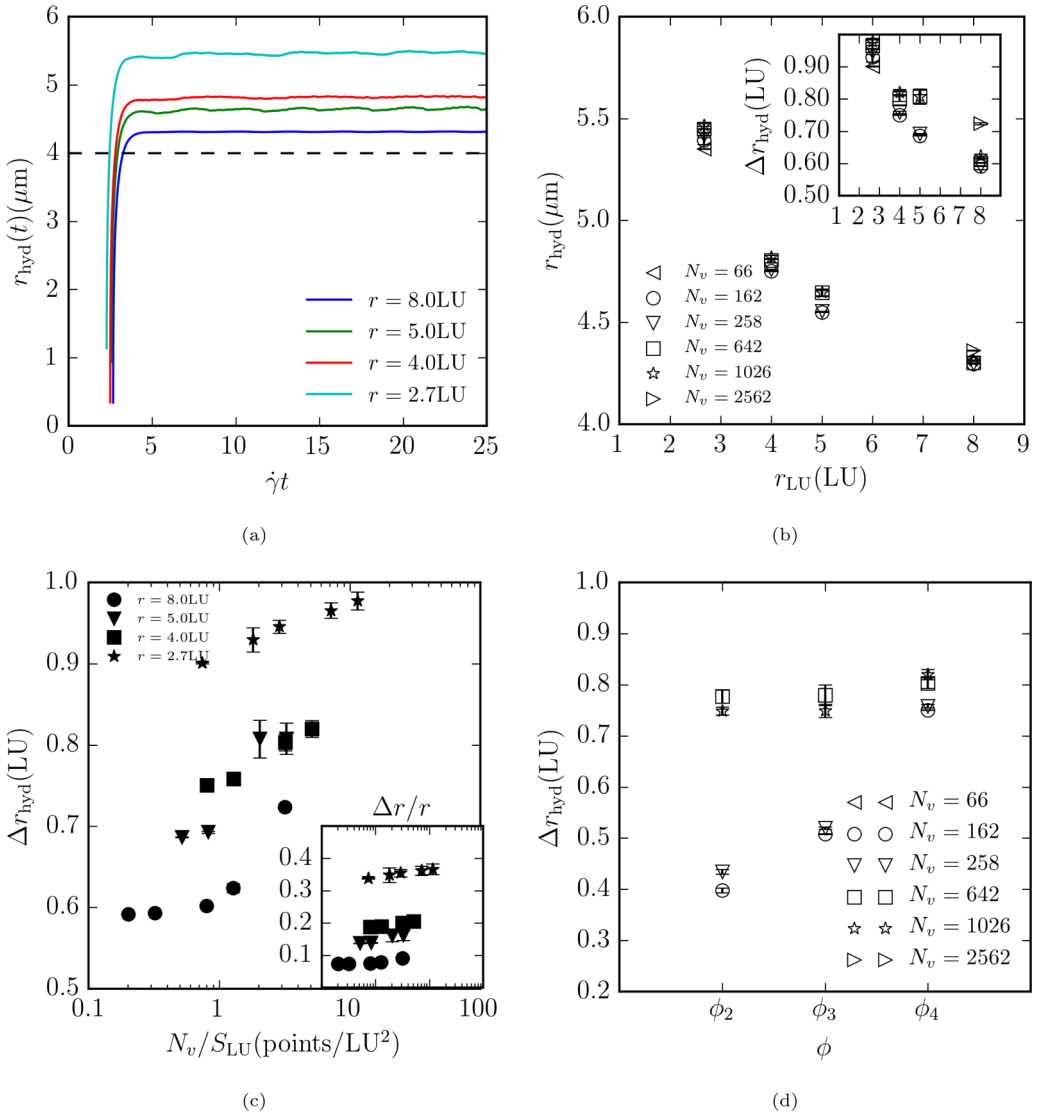

FIG. 3. (a) Evolution of the hydrodynamic radius $r_{\rm hyd}$, as calculated from Eq. (17), with respect to the lattice unit Δx. The horizontal dashed line corresponds to the imposed radius. Finer lattice resolution results in lower effective hydrodynamic radii. (b) Dimensional hydrodynamic vs imposed radius measured in lattice units, varying the number of surface vertices N_v. Inset: same data where the increase $\Delta r_{\rm hyd}$ is now measured in lattice units. (c) Increase in hydrodynamic radius $\Delta r_{\rm hyd}$ in lattice units (LU) with respect to the vertex surface density $N_v/S_{\rm LU}$ ($S_{\rm LU} = 4\pi r^2$). Inset with label $\Delta r/r$: increase in units of radius ($\Delta r_{\rm hyd}/r$) vs surface density $N_v/S_{\rm LU}$. Note that the x axis of the inset is the same as that in the main figure, ranging from 0.1 to 100. (d) Increase in hydrodynamic radius $\Delta r_{\rm hyd}$ with respect to the interpolation kernel ϕ_n, for $r = 4.0$ LU. Vertex numbers of $N_v = 162$ and 258 have a low surface density resulting in smaller $r_{\rm hyd}$, an effect less prevalent in larger interpolation kernels. Adequately resolved spheres produce similar $r_{\rm hyd}$ for all kernels.

This shift corresponds to the migration of neutrally buoyant spherical particles in a Couette flow toward the center of the domain, and it depends on the ratio of the diameter of the particle to the distance between the walls and on the particle-Reynolds number [34]. Kromkamp *et al.* [23] have also noticed an increase in migration with increasing Re_p in their simulations. Our results, however, point to inconsistent behavior regarding this migration. The particle Re used is relatively small ($\sim$0.005) and the domain sufficiently large for this to be a finite-size effect [37]. To quantify this behavior, we define the precollision shift as $\Delta Y_{\rm shift} \equiv \min(\Delta Y_{\Delta X/r<0}) - \Delta Y_0$.

Figure 7(a) suggests that the cases that appeared to be underresolved in the previous cases do not migrate toward the center of the vessel, while migration increases as the vertex density increases. Below the threshold of two vertices per LU^2 there is no migration, suggesting that fluid penetration significantly affects the transport of vesicles in bounded geometries. This is more obvious when using ϕ_2, which does not produce any migration, even in the finer mesh resolutions.

The migration is independent of the relaxation time τ [Fig. 7(c)], while using the Adams-Bashforth scheme produced the same results, thus having no effect in the course of the simulation (data not shown).

3. *Lubrication forces between two spheres*

Finally, we study the lubrication interaction of two spheres. Since the IBM is based on interpolation, the hydrodynamic

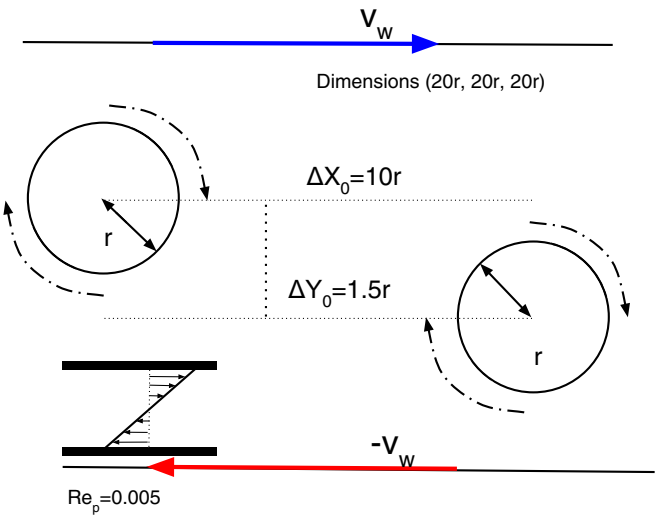

FIG. 4. Schematic for the case described in Sec. III B 1. Two spheres are positioned in a shear-flow environment at rest, and the relative distance between their centers is measured.

interaction of two particles whose surface vertices are close can be accurately resolved up to a certain limit, defined mainly by the support of the kernel and the vertex surface density. Vertices that are close to each other exert force to nearby nodes and interpolate similar velocities, inducing a form of correlation between them. In addition to the overlapping IBM kernels, the fluid flow in their gap cannot be accurately resolved, causing a breakdown of the lubrication force. In this benchmark, we study approaching spheres and lubrication in the normal direction, yet we do not consider rotating spheres and lubrication torque. For particles coupled with the momentum-exchange algorithm (MEA), Nguyen and Ladd [22], based on analytical results of Jeffrey and Onishi [38],

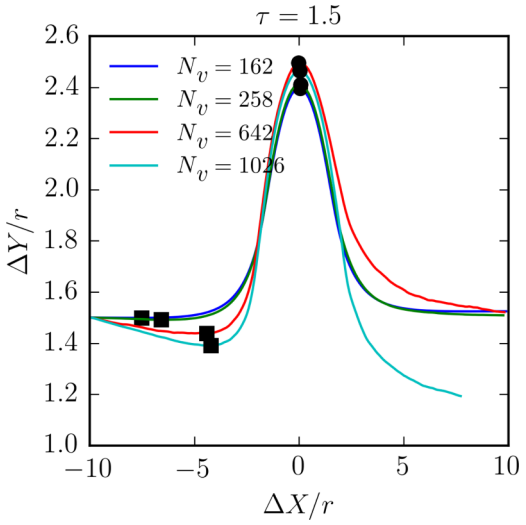

FIG. 5. Flow trajectories for two interacting spheres in shear flow. The number of vertices range from 162 to 1026 for a sphere of 4 LU. • denotes the collision distance $\Delta Y_{\max}$ and ■ denotes the "precollision shift" ΔY_{shift}. Spheres with high resolution ($N_v = 1026$) migrate toward the center of the domain.

proposed a correction for the lubrication force between two spheres with radii r_1 and r_2 when they are closer than a cutoff distance of h_N (assuming forces to be independent of gap, for gaps smaller than h_N):

$$\mathbf{F}_{\text{lub}} = -6\pi\rho\nu\frac{r_1^2 r_2^2}{(r_1+r_2)^2}\left(\frac{1}{h}-\frac{1}{h_N}\right)\mathbf{U}_{12}\cdot\hat{\mathbf{R}}_{12}, \quad h < h_N,$$
$$= 0, \quad h \geqslant h_N. \tag{18}$$

$\mathbf{U}_{12} = \mathbf{U}_1 - \mathbf{U}_2$ refers to the velocity difference between the two spheres, $h = |\mathbf{R}_{12}| - r_1 - r_2$ to the gap between the two surfaces, and $\hat{\mathbf{R}}_{12} = \mathbf{R}_{12}/|\mathbf{R}_{12}|$ is the unit vector connecting the centers of the two spheres. Equation (18) essentially shows that $\mathbf{F}_{\text{lub}}^{\text{normal}} \propto \mathbf{U}_{12}^{\text{normal}}/h$ in the limit of $h \to 0$.

The purpose of these simulations is *not* to propose a lubrication correction scheme for the IBM, but rather to indicate the range in which lubrication is accurately resolved for the IBM surfaces. We use the domain of Sec. III B 1 with $\dot{\gamma} = 0/\text{s}$ and dimensions $(20r \times 20r \times 20r)$ to measure the distance at which the lubrication breaks down. The two spheres are separated by an initial distance of $(\Delta X_0, \Delta Y_0, \Delta Z_0) = (10r, 0, 0)$.

In the scheme we are using, we cannot impose velocity and measure force, as is commonly practiced in these studies [22,24]. Instead, we apply a constant and opposite force of $F_0 = 125$ pN in the x direction on each sphere, and we measure their relative distance. There are several variants of the IBM to simulate rigid bodies, however this would imply using a different scheme, and comparisons with the earlier results would be invalid.

This force may introduce an artificial density difference between the inner and the outer fluid, yet due to the simplicity of the system, potential side effects similar to [24] are considered to be minor, and it is believed that they would not change the outcome considerably. Due to anisotropies in the discretization of the membrane, spheres that are forced may roll over each other and diverge from the head-on collision. To ensure that this will not happen, an additional spring force is considered, keeping the centers of the two spheres aligned with the direction of the force. The force is defined as $\mathbf{F}_{\text{corr}} = (0, -F_0\frac{(Y-Y_0)}{1\ \mu\text{m}}, -F_0\frac{(Z-Z_0)}{1\ \mu\text{m}})$.

4. Results

The quantity we are interested in is the gap h between the two spheres, and in particular h_{fail}, the point where lubrication forces break down (for a description of the definition of h_{fail}, please see Appendix C). Figure 8(b) shows the evolution of h with respect to time. A point is evident, in which the course of the trajectories changes, indicating that the lubrication force is not accurately resolved.

Parameter sets in which spheres have a small effective radius take substantially longer to reach h_{fail}. In our case, these simulations terminate within the designated simulation time before this point. Cases with larger surface density break down at larger distances [see Fig. 9(a)], while h_{fail} seems to be independent of τ, as shown in Fig. 9(b). Deformations of the spheres were negligible. In this benchmark, the use of the Adams-Bashforth scheme had no impact on the results we obtained (data not shown).

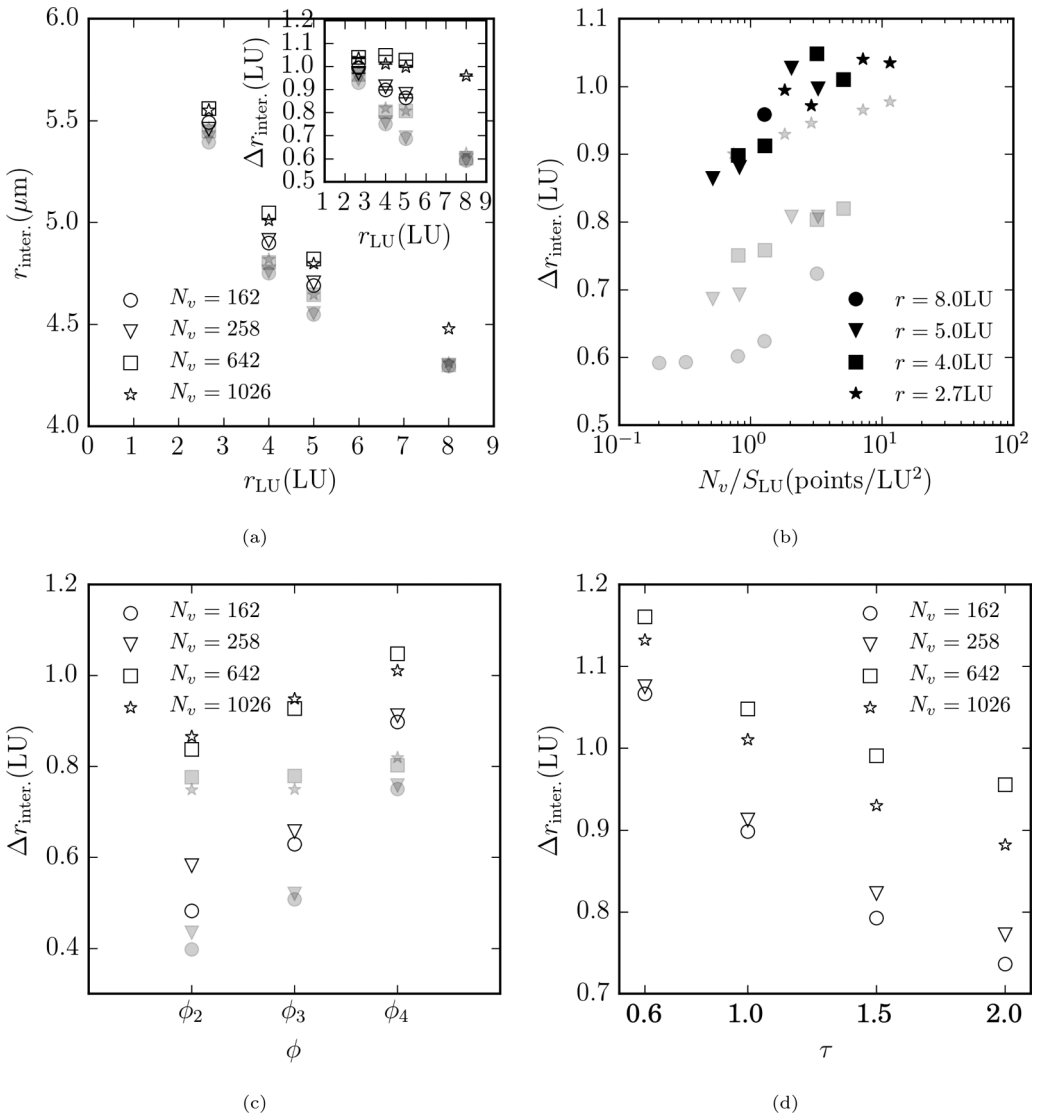

FIG. 6. (a) Dimensional interaction radius vs imposed radius. Transparent symbols correspond to the values measured in Sec. III A. Finer resolutions mitigate the increase in the effective interaction (and hydrodynamic) radius of a sphere. Inset: same data where the increase Δr_{hyd} is now measured in lattice units. (b) Increase in dimensional interaction radius, Δr_{inter}, in lattice units with respect to the vertex surface density N_v/S_{LU}. Transparent symbols correspond to the values measured in Sec. III A. (c) Increase in interaction radius, Δr_{inter}, with respect to the interpolation kernel ϕ_n, for $r = 4.0$ LU. Transparent symbols correspond to the values measured in Sec. III A. Interpolation kernels with larger support increase the interaction radius, while $N_v = 162$ and 258 still appear to result in lower r_{inter} due to the low surface resolution. (d) Increase in interaction radius, Δr_{inter}, with respect to the relaxation time τ, for $r = 4.0$ LU. Increasing τ decreased the interaction radius r_{inter}.

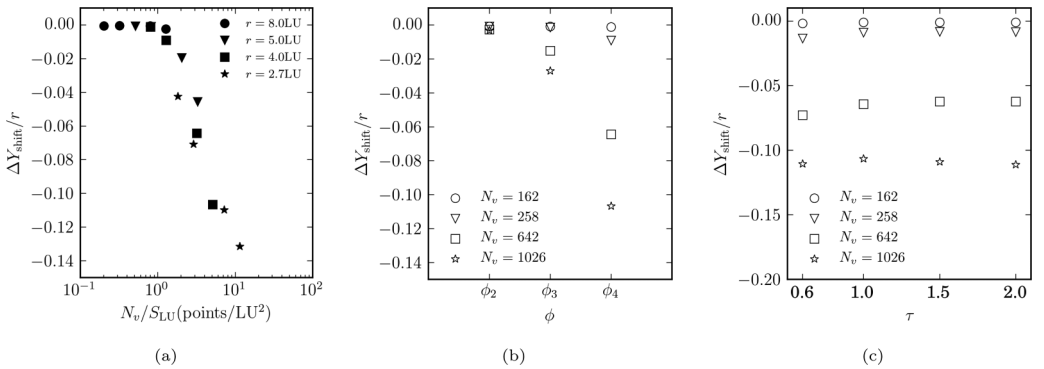

FIG. 7. Normalized precollision shift, $\Delta Y_{\text{shift}}/r$: (a) with respect to the vertex surface density N_v/S_{LU}; (b) with respect to the interpolation kernel ϕ_n; and (c) with respect to the relaxation time τ.

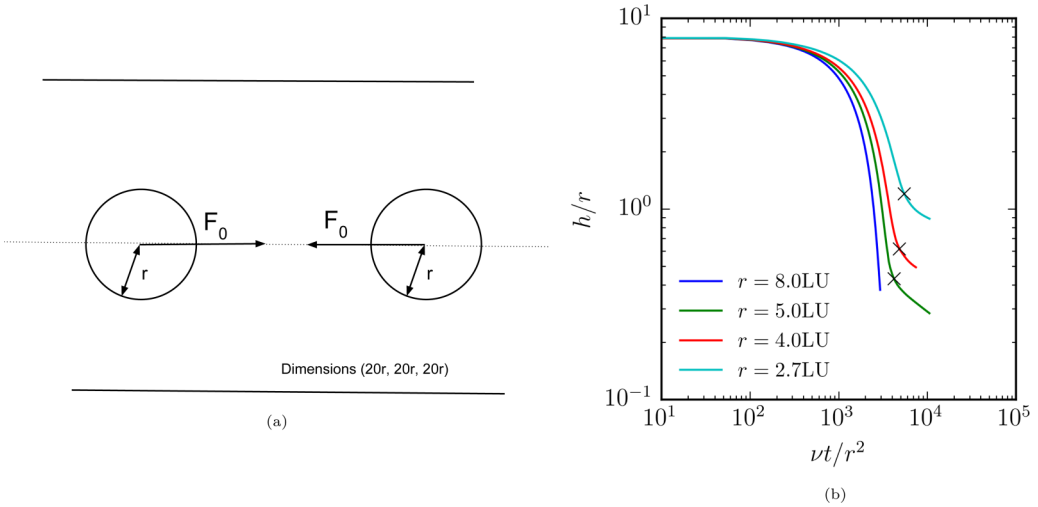

FIG. 8. (a) Schematic for the case described in Sec. III B 3. Two spheres are positioned in a resting fluid and forced toward each other. Their relative positions and gap are measured. (b) Gap h in units of radius, vs dimensionless time, for varying lattice spacings Δx. The symbol $\times$ identifies h_{fail}, the gap in which the lubrication forces fail. In setups with larger effective radii (namely larger Δx), their failure occurs in larger gaps h/r, while they need more time to reach to the same gap.

IV. DISCUSSION

In this work, we present a parametric study for the combined IB-LBM method applied in simulations of one and two suspended particles. We have studied the sensitivity of the simulation results to the lattice constant Δx, the number of vertices N_{v}, the interpolation kernel ϕ, and the LBM relaxation time τ. Computational complexity increases as $\sim f^5$ with a spatial refinement factor f for the LBM subsystem, and $\sim f^2$ for the membrane model from the time step alone without remeshing, and thus the urge to reduce the resolution is high. However, care has to be taken in the choice of parameters since the accuracy of the computations is drastically reduced if mechanical and hydrodynamical interactions are insufficiently resolved. We hope that the presented benchmarks will help other users of the methods to choose the parameters according to the requirements of their applications.

An important conclusion we obtained from the first two benchmarks is that there exists a difference between the radius "felt" by the fluid (i.e., via the stress exerted and measured by r_{hyd}) and the radius "felt" by hydrodynamically interacting spheres. This implies that a consistent effective radius, which could account for the increase, does not exist. Neither r_{hyd} nor r_{inter} can be used to recalibrate the radius of the suspended particle.

In the three benchmarks we have performed, we found that each parameter has its distinct effect on the interaction of the membrane with the fluid and other membranes. Spatial resolution strongly determines the extent of the effective hydrodynamic and lubrication radii of the particle, which, in contrast, are influenced less by membrane-vortex density. In

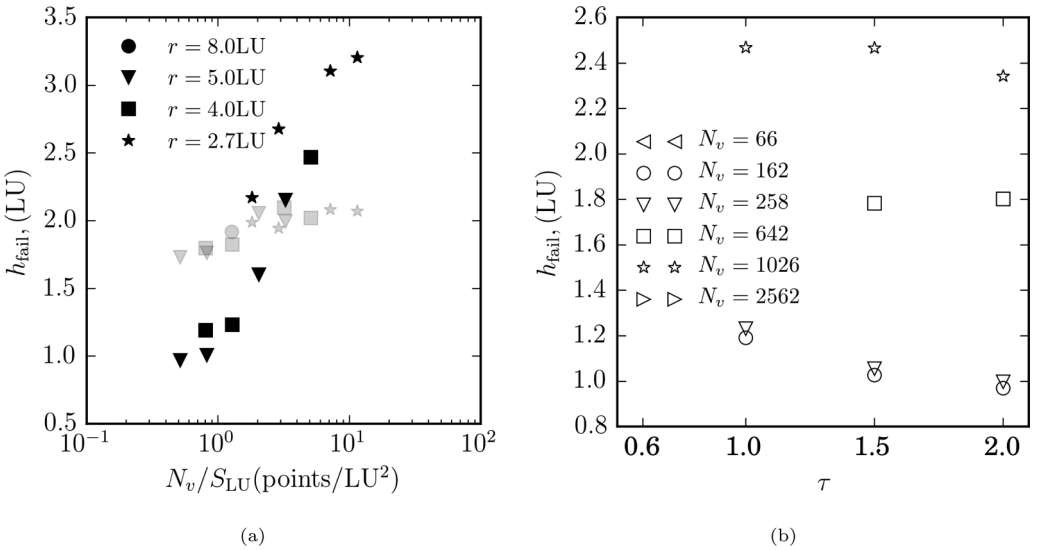

FIG. 9. (a) Failing gap h_{fail} with respect to vertex surface density. Transparent symbols correspond to $2 \times r_{\text{inter}}$. (b) Failing gap h_{fail} with respect to τ.

our simulations we found that mesh resolutions of fewer than two vertices per LU^2 will lead to potential fluid penetration. The effects of underresolved meshes are even more profound for IBM kernels with a smaller support, such as ϕ_2. In the lubrication limit, i.e., for small gaps between the particles, high membrane-vertex density and larger kernels lead to an overestimation of the hydrodynamic interactions. A consistent correction such as that proposed by Nguyen and Ladd [22] for particles coupled to the LBM fluid using the momentum-exchange method would need to take all these effects into account and is not known to date.

Underresolved meshes were also unsuccessful in reproducing the migration of a sphere toward the center of the vessel in a bounded shear flow, thus failing to capture essential physics. This was observed in all cases in which kernel ϕ_2 was used, raising some concerns about whether it captures the relevant physics at all. Using ϕ_4 leads to a more accurate reproduction of the particle migration, highlighting again the importance of mesh resolution. It produces, however, larger effective hydrodynamic radii and fails to resolve the hydrodynamic interaction of two particles in the lubrication limit.

Concluding on a universal set of parameters is not straightforward, and one must differentiate between dilute and dense suspensions. In dilute suspensions, where the mean distance between particles is relatively large, the finer resolutions produce a more accurate response. Interpolation kernel ϕ_2, when the mesh is not properly resolved, appears to be "leaky," in contrast to ϕ_4, which is more robust with respect to the mesh resolution. A particle radius of $r = 4$ LU seems to be sufficient, while the mesh resolution is suggested to be kept above at least 2 points/LU^2 to reproduce the relevant physics. Relaxation time τ does not significantly affect the validity of the method, and since it defines the reach of bounce-back nodes and the time step of the LBM part, it depends on the specific problem. A value of $\tau = 1$ is a good tradeoff between accuracy and efficiency for the LBM.

The strength of ϕ_4 in dilute suspensions is a weakness for the dense case, where the mean interparticle distances are small. Interpolation kernel ϕ_4 has a notable numerical membrane thickness, which leads to the breakdown of the lubrication forces in larger gaps. This could be compensated for by adding an extra *lubrication-correction* force similar to [22,24], yet this exceeds the scope of this paper. In these cases, ϕ_2 with the small numerical thickness can be combined with an adequately resolved mesh to avoid lubrication breakdown. However, if walls are present it is open to question whether the wall-particle interaction would be accurately captured.

Updating the position with the Adams-Bashforth scheme did not yield any differences compared to the Euler scheme, which is simpler and faster and thus preferred over more complex schemes. This was to be expected since LBGK is first-order accurate in time. Higher-order schemes might produce different results.

The number of free parameters is large, and an exhaustive study in three dimensions is challenging, given the low particle-Reynolds numbers and the domain sizes. We explored a parameter space sufficiently large to make the statements above, however further analysis is necessary to identify and understand the various side effects of a combined LBM-IBM scheme. Again, we would like to point out that it is important to perform a series of relevant benchmarks prior to a study in order to validate the choice of parameters.

ACKNOWLEDGMENTS

The authors would like to thank Timm Krüger for fruitful discussions and insightful comments. This research receives funding from the European Union, 7th Framework Programme under Grant Agreement No. 26996 (http://www.thrombus-vph.eu). A.G.H. acknowledges partial financial support by the Russian Scientific Foundation, Grant No. 14-11-00826.

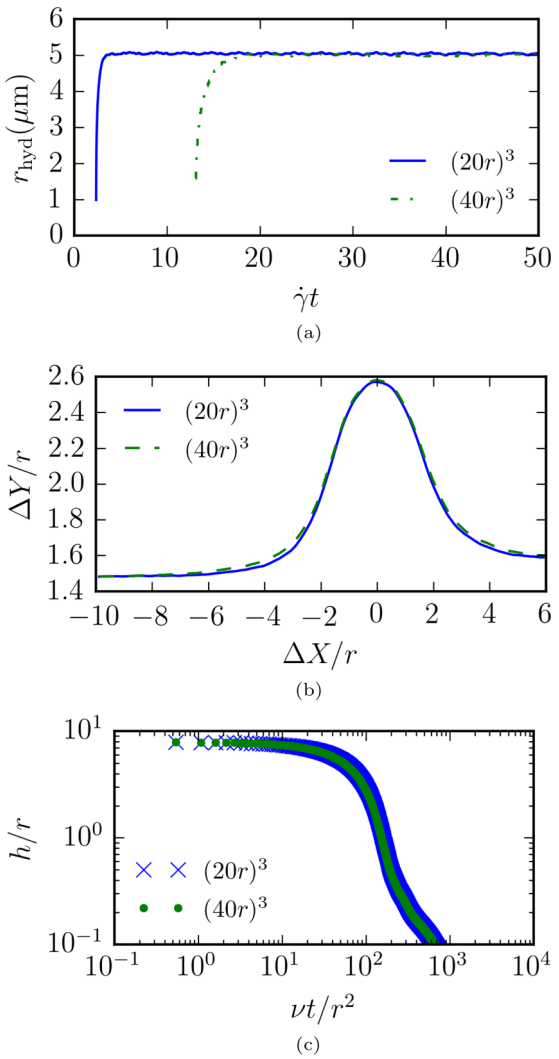

FIG. 10. Finite-size analysis of the cases presented in Sec. III. (a) The case of measuring the hydrodynamic radius from the suspension viscosity. Evolution of the hydrodynamic radius r_{hyd}, as calculated from Eq. (17) with respect to the dimensionless time $\dot{\gamma}t$. The different equilibration times are noticed for the two domain sizes. The values obtained differ by ∼2.7%. (b) The case of two spheres colliding in shear flow. Parametric plot of relative distances in the x and y directions for the two different domain sizes. The values for the calculated r_{inter} between the two domains differ at ∼0.5% of the particle radius. (c) Case of head-on collision of two forced spheres. Evolution of the gap size normalized by the radius for the two different domain sizes. The difference between results from the two domains is within ∼6%.

APPENDIX A: FINITE-SIZE EFFECTS

A finite-size analysis was performed for the results presented in this paper. We compared results for all three cases between the domain used ($20r \times 20r \times 20r$), where r is the radius of the sphere, and by doubling the size of the domain in each direction, namely ($40r \times 40r \times 40r$). Results are presented in Fig. 10. In this analysis, we chose the coarse sphere representation, $r = 2.7$ LU, with $N_v = 258$ vertices, $\tau = 1.0$, and the IBM interpolation kernel ϕ_3. The results obtained, as shown in Fig. 10, are qualitatively and quantitatively very similar. Since the "larger" domain of $40r \times 40r \times 40r$ is eight times more demanding computationally (in terms of time and storage) than the "smaller" domain, the latter was chosen for the simulations.

To conclude, the finite-size analysis produced adequately similar results to justify the use of the smaller domain.

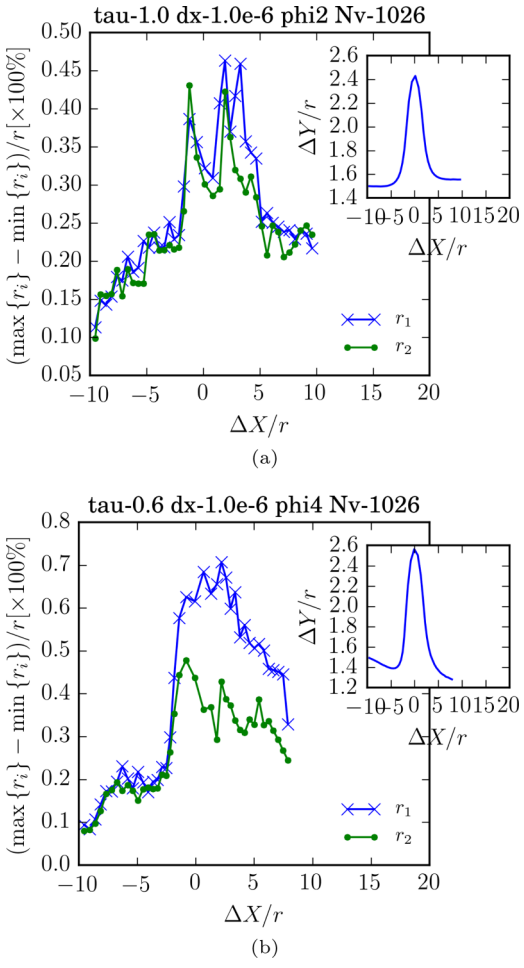

FIG. 11. Departure of the two particles from the spherical shape for the interaction of two spheres in shear flow. Two cases are sampled: (a) one with a minor postcollision displacement and (b) one with a measurable postcollision displacement. The parameters of each simulation are mentioned in the title of each plot, and the inset images depict the relative positions of the two spheres. The deviations are considered to be minor.

APPENDIX B: DEPARTURE FROM THE SPHERICAL SHAPE

In this appendix, we track the deformation of spheres as they collide in shear flow, as presented in Sec. III B 1. The metric used for the deformation is defined as $D = (\max\{r_i\} - \min\{r_i\})/r$, with $r_i = |\mathbf{R}_i - \frac{1}{N_v}\sum_{i=1}^{N_v}\mathbf{R}_i|$ being the distance of vertex i from the center of a sphere with N_v vertices. It is a very sensitive measure and can sense local divergences.

Figures 11(a) and 11(b) track this deformation with respect to the relative distance in the x direction, $\Delta X/r$. These two cases represent one case in which the postcollision migration is negligible [Fig. 11(a)] and one in which it is significant [Fig. 11(b)]. In both of the samples, the deformation D is less than 0.8%, yielding a maximum difference in the radii of the vertices of 0.032 LU. This is considered to be only a minor departure from the spherical shape.

To conclude, no significant deviation from the spherical shape was observed for the cases considered, rendering the objects we used spherical.

APPENDIX C: METRIC FOR LUBRICATION FAILURE

Defining the gap h_{fail}, in which the lubrications fail, is not a straightforward task. The radii of the spheres are not exact, and methods other than using Eq. (18) have to be employed. We have noticed in the log-log plot of the gap versus time [like Fig. 8(b)] that after failure, it becomes linear in log-log space with an exponent n, which is $-1 < n < 0$. The exponent before can be seen as less than -1, hence if multiplied by time t, quantity ht can be used to distinguish the two regimes, as shown in Fig. 12(a).

By visual inspection, we verified that the gaps h_{fail} have been identified correctly in the cases presented.

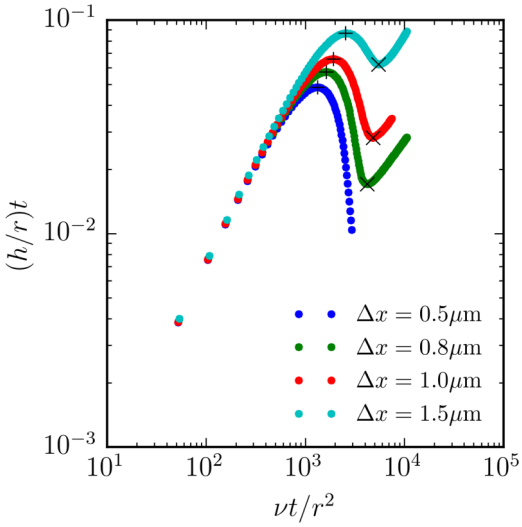

FIG. 12. Quantity ht/r, used to identify h_{fail}. The symbol $\times$ identifies h_{fail} as the local minimum of this quantity, while $+$ identifies the first local maximum.

[1] E. A. Fadlun, R. Verzicco, P. Orlandi, and J. Mohd-Yusof, Combined immersed-boundary finite-difference methods for three-dimensional complex flow simulations, J. Comput. Phys. **161**, 35 (2000).

[2] F.-B. Tian, H. Luo, L. Zhu, J. C. Liao, and X.-Y. Lu, An efficient immersed boundary-lattice Boltzmann method for the hydrodynamic interaction of elastic filaments, J. Comput. Phys. **230**, 7266 (2011).

[3] J. Zhang, P. C. Johnson, and A. S. Popel, Effects of erythrocyte deformability and aggregation on the cell free layer and apparent viscosity of microscopic blood flows, Microvasc. Res. **77**, 265 (2009).

[4] L. Crowl and A. L. Fogelson, Analysis of mechanisms for platelet near-wall excess under arterial blood flow conditions, J. Fluid Mech. **676**, 348 (2011).

[5] L. Mountrakis, E. Lorenz, and A. G. Hoekstra, Where do the platelets go? A simulation study of fully resolved blood flow through aneurysmal vessels, Interface Focus **3**, 20120089 (2013).

[6] L. Mountrakis, E. Lorenz, and A. G. Hoekstra, Validation of an efficient two-dimensional model for dense suspensions of red blood cells, Int. J. Mod. Phys. C **25**, 1441005 (2014).

[7] L. Mountrakis, E. Lorenz, and A. G. Hoekstra, Scaling of shear-induced diffusion and clustering in a blood-like suspension, Europhys. Lett. **114**, 14002 (2016).

[8] T. Kruger, M. Gross, D. Raabe, and F. Varnik, Crossover from tumbling to tank-treading-like motion in dense simulated suspensions of red blood cells, Soft Matter **9**, 9008 (2013).

[9] C. S. Peskin, Flow patterns around heart valves: A numerical method, J. Comput. Phys. **10**, 252 (1972).

[10] C. S. Peskin, The immersed boundary method, Acta Numer. **11**, 479 (2002).

[11] M. Uhlmann, An immersed boundary method with direct forcing for the simulation of particulate flows, J. Comput. Phys. **209**, 448 (2005).

[12] T. Kempe and J. Fröhlich, An improved immersed boundary method with direct forcing for the simulation of particle laden flows, J. Comput. Phys. **231**, 3663 (2012).

[13] X. Yang, X. Zhang, Z. Li, and G.-W. He, A smoothing technique for discrete delta functions with application to immersed boundary method in moving boundary simulations, J. Comput. Phys. **228**, 7821 (2009).

[14] J. Wu and C. Shu, Implicit velocity correction-based immersed boundary-lattice boltzmann method and its applications, J. Comput. Phys. **228**, 1963 (2009).

[15] L. Mountrakis, E. Lorenz, O. Malaspinas, S. Alowayyed, B. Chopard, and A. G. Hoekstra, Parallel performance of an IB-LBM suspension simulation framework, J. Computat. Sci. **9**, 45 (2015).

[16] M. Gross, T. Krüger, and F. Varnik, Fluctuations and diffusion in sheared athermal suspensions of deformable particles, Europhys. Lett. **108**, 68006 (2014).

[17] T. Krüger, F. Varnik, and D. Raabe, Efficient and accurate simulations of deformable particles immersed in a fluid using a combined immersed boundary lattice boltzmann finite element method, Comput. Math. Appl. **61**, 3485 (2011).

[18] T. Krüger, B. Kaoui, and J. Harting, Interplay of inertia and deformability on rheological properties of a suspension of capsules, J. Fluid Mech. **751**, 725 (2014).

[19] G. K. Batchelor and J. T. Green, The hydrodynamic interaction of two small freely-moving spheres in a linear flow field, J. Fluid Mech. **56**, 375 (1972).

[20] F. R. Da Cunha and E. J. Hinch, Shear-induced dispersion in a dilute suspension of rough spheres, J. Fluid Mech. **309**, 211 (1996).

[21] M. Lopez and M. D. Graham, Shear-induced diffusion in dilute suspensions of spherical or nonspherical particles: Effects of irreversibility and symmetry breaking, Phys. Fluids (1994-present) **19**, 073602 (2007).

[22] N. Q. Nguyen and A. J. C. Ladd, Lubrication corrections for lattice-Boltzmann simulations of particle suspensions, Phys. Rev. E **66**, 046708 (2002).

[23] J. Kromkamp, D. T. M. van den Ende, D. Kandhai, R. G. M. van der Sman, and R. M. Boom, Shear-induced self-diffusion and microstructure in non-Brownian suspensions at non-zero reynolds numbers, J. Fluid Mech. **529**, 253 (2005).

[24] E. Lorenz, A. Caiazzo, and A. G. Hoekstra, Corrected momentum exchange method for lattice Boltzmann simulations of suspension flow, Phys. Rev. E **79**, 036705 (2009).

[25] S. Succi, *The Lattice Boltzmann Equation for Fluid Dynamics and Beyond (Numerical Mathematics and Scientific Computation)*, 1st ed. (Oxford University Press, Oxford, 2001).

[26] Z. Guo, C. Zheng, and B. Shi, Discrete lattice effects on the forcing term in the lattice Boltzmann method, Phys. Rev. E **65**, 046308 (2002).

[27] http://www.palabos.org.

[28] I. V. Pivkin and G. E. Karniadakis, Accurate Coarse-Grained Modeling of Red Blood Cells, Phys. Rev. Lett. **101**, 118105 (2008).

[29] D. A. Reasor, J. R. Clausen, and C. K. Aidun, Coupling the lattice-Boltzmann and spectrin-link methods for the direct numerical simulation of cellular blood flow, Int. J. Numer. Meth. Fluids **68**, 767 (2012).

[30] D. A. Fedosov, B. Caswell, and G. E. Karniadakis, Systematic coarse-graining of spectrin-level red blood cell models, Comput. Methods Appl. Mech. Eng. **199**, 1937 (2010).

[31] G. Le and J. Zhang, Boundary slip from the immersed boundary lattice Boltzmann models, Phys. Rev. E **79**, 026701 (2009).

[32] A. J. C. Ladd, Numerical simulations of particulate suspensions via a discretized boltzmann equation. Part i. Theoretical foundation, J. Fluid Mech. **271**, 285 (1994).

[33] X. He, Q. Zou, L.-S. Luo, and M. Dembo, Analytic solutions of simple flows and analysis of nonslip boundary conditions for the lattice boltzmann BGK model, J. Stat. Phys. **87**, 115 (1997).

[34] P. Vasseur and R. G. Cox, The lateral migration of a spherical particle in two-dimensional shear flows, J. Fluid Mech. **78**, 385 (1976).

[35] A. Kumar and M. D. Graham, Margination and segregation in confined flows of blood and other multicomponent suspensions, Soft Matter **8**, 10536 (2012).

[36] A. J. C. Ladd, Numerical simulations of particulate suspensions via a discretized boltzmann equation. Part 2. Numerical results, J. Fluid Mech. **271**, 311 (1994).

[37] The dimensions of the system were doubled and yielded the same effects, while simulating each sphere individually also produced a migration toward the center (data not shown).

[38] D. J. Jeffrey and Y. Onishi, Calculation of the resistance and mobility functions for two unequal rigid spheres in low-Reynolds-number flow, J. Fluid Mech. **139**, 261 (1984).